

## RETRIEVING TOPOLOGICAL INFORMATION FOR PHASE FIELD MODELS\*

QIANG DU<sup>†</sup>, CHUN LIU<sup>†</sup>, AND XIAOQIANG WANG<sup>†</sup>

**Abstract.** The phase field approach has become a popular tool in modeling interface motion, microstructure evolution, and more recently the shape transformation of vesicle membranes under elastic bending energy. While it is advantageous to employ phase field models in numerical simulations to automatically handle topological changes to the microstructures or the configurations of vesicle membranes, detecting topological events may also become important for many applications such as those in the simulation of blood cells. Motivated by such considerations, a new quantity is formulated to retrieve some topological information based on the phase field formulation and to capture the occurrence of topological events. It can also be used as a control method to avoid unphysical changes of topology due to the numerical methods, should it become necessary for particular practical applications. Through numerical experiments, we demonstrate the effectiveness and the robustness of the new quantity in detecting the topology of fluid bubbles and vesicle membranes.

**Key words.** phase field, elastic bending energy, Gauss–Bonnet formula

**AMS subject classifications.** 57M50, 74A50, 74S99, 92C05

**DOI.** 10.1137/040606417

**1. Introduction.** Phase field modeling of mesoscopic morphology and microstructure evolution has become popular in recent years (see [6, 7, 8, 9, 12, 13, 21, 22, 24, 34, 35, 38, 39] and the references therein). These phase field approaches are usually combined with energetic variational formulations that lead to a diffuse interface modeled by a mixing energy. This allows topological changes of the interface to take place naturally [28, 31, 37]. Such a feature gives such approaches many advantages in numerical simulation of the interface variation and the interfacial motion (cf. [11]). More recently, we have given another successful application of the phase field model for computing the equilibrium configurations of vesicle membranes that minimize the bending elastic energy [19, 18]. The methods developed in [19] can be very useful in morphological studies of vesicle membranes under elastic bending energy, which has many interesting applications.

In this paper, we continue the study of the phase field model but from a different, and perhaps also very novel, point of view. We are motivated by the fact that in many engineering and biological applications, such as the modeling of blood cells in vascular systems, topological information about the vesicle membranes is of critical value. Thus, how to detect and control the topological change of the interface in the phase field modeling and numerical simulation becomes an important issue. Partly due to the nature of the phase field method (and all other level set methods) in their standard formulation, there is no mechanism preventing the topological change of the membranes or other interfaces. In fact, some of the topological changes are due purely to the formulations, instead of the underlying physics. To our knowledge, there has not

---

\*Received by the editors April 7, 2004; accepted for publication (in revised form) January 13, 2005; published electronically August 3, 2005. The research of the first and third authors was supported in part by NSF-DMR 0205232, NSF-DMS 0196522, and NSF-DMS 0400297. The research of the second author was supported by NSF-DMS 040850 and NSF-DMS 0509094.

<http://www.siam.org/journals/siap/65-6/60641.html>

<sup>†</sup>Department of Mathematics, Pennsylvania State University, University Park, PA 16802 (qdu@math.psu.edu, liu@math.psu.edu, wang@math.psu.edu).

been any discussion in the literature on how to recover relevant topological information from the phase field simulations, nor to address further control mechanisms.

The general phase field model is based on the introduction of a phase function (or order parameter)  $\phi = \phi(x)$ , defined on the physical (computational) domain  $\Omega$  that encloses  $\Gamma$ . The function  $\phi$  is used to label the inside and the outside of the vesicle  $\Gamma$ : the level set  $\{x : \phi(x) = 0\}$  gives the membrane, while  $\{x : \phi(x) > 0\}$  represents the interior of the membrane and  $\{x : \phi(x) < 0\}$  the exterior. A *transition thickness* parameter is also chosen to characterize the typical length scale of the transition layer (or the thickness of the *regularized* diffuse interface). For time dependent problems, it is natural to allow  $\phi = \phi(x, t)$ . The objective of our study here is to propose some robust and efficient methods for retrieving or recovering interesting topological information within the phase field framework. In particular, we will develop some robust formulae for computing the Euler number for the modeled interface based on order parameter  $\phi$ .

We expect that our study here has the potential of opening up a host of exciting new applications of phase field modeling, including the use of the topological quantities in a control setting. Our numerical simulation indicates that the generalized Euler number ( $\frac{\chi}{2}$  in three dimensions and  $\chi$  in two dimensions) not only is a better indicator of topological changes than the energy functional we had been using in our previous paper [19], but in fact, gives a quantized jump upon a completion of the topological change (a direct consequence of the Gauss–Bonnet formula) for regular surfaces. Moreover, when the computed surface passes singularity, the new formula for  $\chi$  based on the phase field formulation gives a fractional interpolation of the usual Euler number.

The study of the Euler number in terms of  $\chi$ , or the Euler–Poincaré index number  $\eta$ , may provide guidance for the study of other topological quantities within the phase field framework. The ideas proposed in this paper may be equally applicable to other simulation methods for free boundary and interface problems such as the level set methods. Our work here is also likely to shed light on the study of many geometrical modeling problems, where providing topological information or controlling topological changes may be highly desirable.

The rest of the paper is organized as follows. In section 2, we briefly recall the phase field model, and we discuss a formulation of the Euler number (in terms of  $\chi$ ) within the phase field framework that can be used to recover some topological information. We present a set of formulae in various three-dimensional (3-D) and two-dimensional (2-D) cases. We also discuss the Euler–Poincaré index number  $\eta$  when the surfaces involve singularities. In section 4, we illustrate the method of computing the quantity  $\chi$  in two applications and demonstrate the effectiveness and the robustness of the our formulation. Finally, some concluding remarks are given in section 5.

**2. The Euler number.** Given an oriented (regular) compact (i.e., without boundary) surface  $\Gamma$ , the well-known Gauss–Bonnet formula states that

$$(2.1) \quad \int_{\Gamma} K \, ds = 2\pi\chi,$$

where  $K = k_1 k_2$  is the Gaussian curvature of the surface in  $R^3$ ,  $ds$  is the area element, and  $\frac{\chi}{2}$  in three dimensions ( $\chi$  in two dimensions) is the Euler number [16]. The number  $\chi$  is a commonly used topological quantity. For some frequently encountered surfaces, we have  $\chi = 2$  for a sphere,  $\chi = 0$  for a torus, and  $\chi = -2$  for a torus with two holes.

For 2-D curves,  $K$  is the curvature and  $\chi = 1$  for a circle. For convenience, in this paper we call  $\frac{\chi}{2}$  the Euler number in 3-D cases and  $\chi$  in 2-D cases.

In this section, it is our goal to find a suitable expression of the Euler number when the surface is implicitly defined by a phase field formulation. We first give the general formula of the Euler number under a general phase field definition for both 2-D and 3-D spaces. Then we give some simplified formulae under some specific ansatz assumptions corresponding to our applications. For simplicity, we focus on only the static case when deriving the formulae. In the time dependent case, since we are mostly interested in the topological information of a spatially distributed interface at a fixed time stance, the generalizations to time dependent problems are obvious.

We note that many of our derivations are through formal asymptotics, though more detailed and more rigorous justifications will be provided in our subsequent work [17].

**2.1. The 3-D case.** Let  $\Gamma$  be a smooth oriented compact surface in a domain  $\Omega$  in  $\mathbf{R}^3$ ; we note that  $\Gamma$  is allowed to have multiple disconnected pieces. Let  $p$  be a monotone increasing function defined from  $\mathbf{R}$  to  $\mathbf{R}$  with  $p(0) = 0$ . For each function  $p$ , we take a phase field function  $\phi = \phi(x)$  of  $\Omega$  as  $\phi(x) = p(d(x, \Gamma))$  where the signed distance function  $d = d(x, \Gamma)$  is defined to be positive inside  $\Omega$  and negative outside  $\Omega$ . The level sets of  $\phi$  are denoted by  $\Gamma_\mu = \{x \in \Omega | \phi(x) = \mu\}$ . In particular, we have  $\Gamma = \Gamma_0$ . We also define  $\Omega(a, b) = \{x \in \Omega | b < \phi(x) < a\}$ , which forms a banded (layered) neighborhood around the surface for  $b < 0 < a$ .

Define  $\Lambda(M) = \text{Tr}(\text{Adj}(M))$  for a matrix  $M$ . Clearly,  $\Lambda(M)$  is the coefficient of the linear term of the characteristic polynomial of  $M$ . In particular, for the singular matrix  $M = \nabla^2 d$  we have  $\Lambda(M) = \lambda_1(M)\lambda_2(M)$ , with  $\lambda_1$  and  $\lambda_2$  being the two nonzero eigenvalues of  $M$ .

**THEOREM 2.1.** *Using the notation above, for any monotone increasing function  $p$  there exists  $b < 0 < a$  such that the matrix  $M$ , defined by*

$$(2.2) \quad M(x)_{ij} = \frac{1}{2\sqrt{\pi(a-b)|\nabla\phi|}} \left( \nabla_i \nabla_j \phi - \frac{\nabla|\nabla\phi|^2 \cdot \nabla\phi}{2|\nabla\phi|^4} \nabla_i \phi \nabla_j \phi \right),$$

*is a singular matrix for any  $x \in \Omega(a, b)$  and the Euler number of  $\Gamma$  is given by*

$$(2.3) \quad \frac{\chi}{2} = \int_{\Omega(a,b)} \Lambda(M(x)) dx.$$

*Proof.* Since  $\phi$  depends only on the distance  $d$ , and  $p$  is monotone increasing, there exist real numbers  $a$  and  $b$ , with  $b < 0 < a$ , sufficiently close to 0 such that  $\Gamma_\mu$  are close to the parallel translations of  $\Gamma$  in the normal direction for all  $b \leq \mu \leq a$ , and all  $\Gamma_\mu$  have the same topology as  $\Gamma$ .

Direct computation shows

$$\nabla_i \nabla_j d = \frac{\nabla^2 \phi}{p'} - \frac{p''}{p'} \nabla_i d \nabla_j d = \frac{1}{p'} [\nabla_i \nabla_j \phi - p'' \nabla_i d \nabla_j d].$$

The matrix  $\nabla^2 d$ , with  $d = d(x, \Gamma)$  being the signed distance from  $x$  to the surface  $\Gamma$ , always has a zero eigenvalue with  $\nabla d$  as the eigenvector. This is due to the fact that  $\nabla^2 d$  is symmetric and  $|\nabla d| = 1$ . On the surface  $\Gamma$ , the two other eigenvalues are actually the two principle curvatures of  $\Gamma$  ( $k_1$  and  $k_2$  in this case). The Gaussian curvature  $K$  is of course the product of these two eigenvalues, while the mean curvature  $H$  is

given by the mean of the two eigenvalues. Both quantities can in fact be defined and computed on all the level sets in  $\Omega(a, b)$ . For instance, the Gaussian curvature  $K$  can be conveniently computed from  $\text{Tr}(\text{Adj}(\nabla^2 d))$  (the sum of the three principal  $2 \times 2$  minors of  $\nabla^2 d$ ; see section 2.6 for an example in the cylindrically symmetric case).

Assuming that  $k_1$  and  $k_2$  remain constant along the normal directions in  $\Omega'$ , we have

$$\begin{aligned}
 \frac{\chi}{2} &= \frac{1}{4\pi} \int_{\Gamma} k_1(x)k_2(x) \, ds \\
 &= \frac{1}{4\pi(a-b)} \int_{p^{-1}(b)}^{p^{-1}(a)} p'(\tau) d\tau \int_{\Gamma} k_1(x)k_2(x) \, ds \\
 (2.4) \quad &= \frac{1}{4\pi(a-b)} \int_{\Omega(a,b)} p'(d(x, \Gamma))k_1(x)k_2(x) \, dx \\
 &= \frac{1}{4\pi(a-b)} \int_{\Omega(a,b)} p'(d(x, \Gamma))\Lambda(\nabla^2 d(x, \Gamma)) \, dx \\
 (2.5) \quad &= \frac{1}{4\pi(a-b)} \int_{\Omega(a,b)} \frac{1}{p'(d(x, \Gamma))} \Lambda(\nabla^2 \phi - p''\nabla_i d \nabla_j d) \, dx.
 \end{aligned}$$

Now, since  $p$  is monotone increasing, we have  $p'(d(x, \Gamma)) = |\nabla\phi(x)|$  and

$$p''(d(x, \Gamma)) = \nabla|\nabla\phi| \cdot \frac{\nabla\phi}{|\nabla\phi|}(x) = \frac{\nabla|\nabla\phi|^2 \cdot \nabla\phi}{2|\nabla\phi|^2}(x).$$

Hence we get the general formula for the Euler number in three dimensions:

$$\begin{aligned}
 (2.6) \quad \frac{\chi}{2} &= \frac{1}{4\pi(a-b)} \int_{\Omega(a,b)} \frac{1}{|\nabla\phi|} \Lambda \left( \nabla_i \nabla_j \phi - \frac{\nabla|\nabla\phi|^2 \cdot \nabla\phi}{2|\nabla\phi|^4} \nabla_i \phi \nabla_j \phi \right) \, dx \\
 &= \frac{1}{4\pi(a-b)} \int_{\Omega(a,b)} \frac{1}{|\nabla\phi|} \Lambda(M(x)) \, dx.
 \end{aligned}$$

From the definitions of  $M$  and  $\Lambda(M)$ , we know that  $M(x)$  is singular for any  $x \in \Omega(a, b)$  in the sense that it always has a zero eigenvalue, and (2.3) holds.  $\square$

The formula (2.3) forms the basis for our efforts to recover topological information, in particular the Euler number.

**2.2. The 2-D case.**

**THEOREM 2.2.** *If  $\Omega \in \mathbf{R}^2$ , with the same notation as in Theorem 2.1, for any monotone increasing function  $p$  there exists  $b < 0 < a$  such that*

$$(2.7) \quad \chi = \frac{1}{2\pi(a-b)} \int_{\Omega(a,b)} \left( -\Delta\phi + \frac{\nabla|\nabla\phi|^2 \cdot \nabla\phi}{2|\nabla\phi|^2} \right) \, dx.$$

*Proof.* Using the same argument as above, this can be derived as follows:

$$\begin{aligned}
 \chi &= \frac{1}{2\pi} \int_{\Gamma} K(x) \, ds \\
 &= \frac{1}{2\pi(a-b)} \int_{\Omega(a,b)} p'(d(x, \Gamma))K(x) \, dx \\
 &= \frac{1}{2\pi(a-b)} \int_{\Omega(a,b)} (-\Delta\phi + p''(d(x, \Gamma))) \, dx \\
 (2.8) \quad &= \frac{1}{2\pi(a-b)} \int_{\Omega(a,b)} \left( -\Delta\phi + \frac{\nabla|\nabla\phi|^2 \cdot \nabla\phi}{2|\nabla\phi|^2} \right) \, dx. \quad \square
 \end{aligned}$$

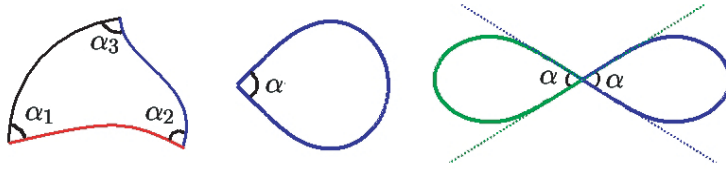


FIG. 2.1. *Singular 2-D cases.*

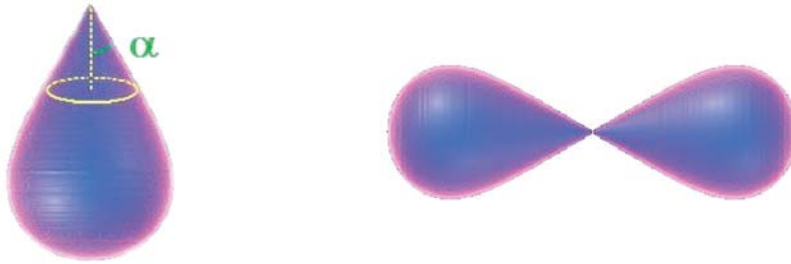


FIG. 2.2. *Singular 3-D cases.*

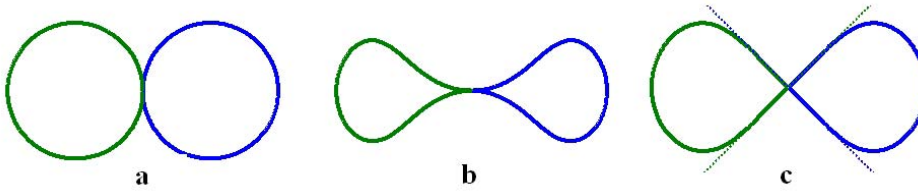


FIG. 2.3. *Singular 2-D cases. The inner intersect angles are  $\pi$ ,  $0$ ,  $\pi/2$  for cases a, b, and c, respectively.*

**2.3. Cases involving singularities on the interfaces.** Both Theorems 2.1 and 2.2 require that  $\Gamma$  be a smooth oriented compact surface. However, in realistic physical applications, we always encounter the singular cases where either the curves or the surfaces intersect or have some sharp angles or cones. Figure 2.1 illustrates several simple singular cases in two dimensions, while Figure 2.2 shows two singular shapes in three dimensions.

With the possible occurrence of the singularities, we will employ the general Gauss–Bonnet formula. In the 2-D case, suppose that the curves are piecewise smooth with  $n$  vertices (sharp corners) and that the inner angles for each vertices are  $\{\alpha_i, i = 1, \dots, n\}$ . The Gauss–Bonnet formula reads as

$$2\pi\eta = \int_{\Gamma} K ds + \sum_{i=1}^n (\pi - \alpha_i) = 2\pi\chi + \sum_{i=1}^n (\pi - \alpha_i),$$

where  $\eta$ , the Euler–Poincaré index number, is the topological integer, the genus of the surface [16].

We give illustrations, in Figures 2.1 and 2.3, of the values of  $\chi$  defined by  $2\pi\chi = \int_{\Gamma} K ds$  in the singular cases. For configurations such as the third image in Figure

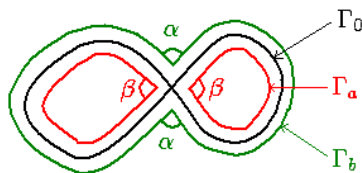


FIG. 2.4.  $\Gamma_0$ ,  $\Gamma_a$ , and  $\Gamma_b$  have different topologies but the same Euler number.

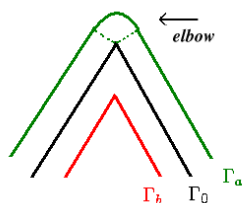


FIG. 2.5. By getting rid of the singular complement,  $\Gamma_0$ ,  $\Gamma_a$ , and  $\Gamma_b$  have the same Euler number.

2.1,  $2\pi\eta = \int_{\Gamma} K ds + 2(\pi - \alpha)$ . In particular, for the cases in Figure 2.3,  $\alpha = \pi, 0, \frac{\pi}{2}$  for the cases a, b, and c, respectively. In all of these cases, the Euler–Poincaré index number  $\eta$  is always 2, representing the number of bubbles.

On the other hand, the value of  $\chi$  can be used to detect the change of topology even with the presence of the singular cases. Again, using the example in Figure 2.3, the Euler numbers  $\chi$  are 2, 1, and 1.5, respectively, with the singularity being signaled by the fractional value. We want to point out that in the first case, the Euler number  $\chi$  is still equal to the Euler–Poincaré index number  $\eta$ , even with the singularity.

When we consider the definition of  $\chi$  for the 3-D singular cases, we may also get a fractional Euler number when singularity appears. For example, for the configuration in the first picture of Figure 2.2, suppose that the angle of the tangent cone is  $\alpha$ ; the Euler number can be derived from the following explicit analytic formula by calculating the ratio between the spherical cap cut by the  $\alpha$ -cone and the total area of the sphere:

$$(2.9) \quad \frac{\chi}{2} = \frac{1}{4\pi} \int_{\Gamma} K ds = 1 - \frac{1}{4\pi} (2\pi(1 - \sin \alpha)) = \frac{1}{2} + \frac{1}{2} \sin \alpha.$$

Finally, we discuss the validity of formulae (2.3) and (2.7) in singular cases. Figure 2.4 shows that  $\Gamma_{\mu}$  seem to have (visual) topology different from that of  $\Gamma$  for some  $b < \mu < a$ .

However, in reference to Figure 2.4, because each  $\Gamma_{\mu}$  has a singular vertex with angle either  $\alpha$  or  $\beta = \pi - \alpha$ , the Euler number  $\xi$  for every  $\Gamma_{\mu}$  is the same as that of  $\Gamma_0$ . Thus Theorems 2.1 and 2.2 still hold for this singular case where the Euler number is a fractional number.

One will encounter the issue of a *singular complement* in the numerical simulations of the interfaces involving singularities. This is crucial in calculating the fractional Euler number correctly. To clarify this phenomenon, let us examine Figure 2.5.

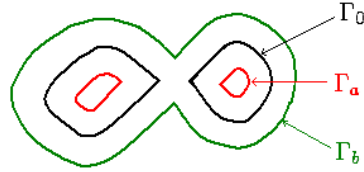


FIG. 2.6. An illustration of the choice of  $a$  and  $b$ .  $\Gamma_0$ ,  $\Gamma_a$ , and  $\Gamma_b$  have the same Euler number.

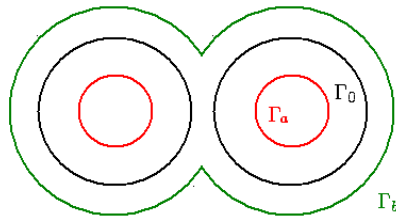


FIG. 2.7.  $\Gamma_0$ ,  $\Gamma_b$  have different Euler numbers.

Because of the *elbow* shape associated with  $\Gamma_a$ ,  $\Gamma_a$  has a different Euler number from  $\Gamma_0$ . This phenomenon, hereafter referred to as the *singularity compensation*, occurs in all numerical experiments involving interfacial singularities due to the numerical smoothing of the surfaces. This appears to introduce difficulties into the application of Theorems 2.1 and 2.2. However, noticing that the elbow has very large curvature, if a method can be designed to filter out such an elbow, the Euler number calculated for the remaining  $\Gamma_a$  would remain the same as that of  $\Gamma_0$ . Such a technique will be introduced and developed later in section 3.

**2.4. Stability and autoselection of parameters.** Although the proofs of Theorems 2.1 and 2.2 are given under the condition that for every  $b < \mu < a$ ,  $\Gamma_\mu$  has the same topology as  $\Gamma_0$ , to correctly identify the Euler number, one can relax such a condition to requiring that the Euler number of  $\Gamma_\mu$  be the same as that of  $\Gamma_0$ . By the analysis of section 2.3, it is desirable that the parameters  $a$  and  $b$  are chosen to be quite different from 0. Figure 2.6 gives an illustration of such a case.

The advantage of choosing  $a$  and  $b$  some distance away from 0 is to ensure that  $\Omega(a, b)$  contains plenty of grid points, which in turn makes the integration for the Euler number more accurate and stable.

However, in general, it is not true that all the neighboring curves or surfaces always share the same Euler number. In Figure 2.7,  $\Gamma_0$  and  $\Gamma_b$  clearly have different Euler numbers. The largest  $b$  can be selected only where the two circles of  $\Gamma_b$  are tangent to each other. How to choose the value of  $b$  in such situations becomes a very relevant issue in our computation of the Euler numbers.

On the other hand, in Figure 2.7, we may notice that  $\Gamma_a$  always has the same Euler number as  $\Gamma_0$ , and  $a$  can be very different from 0. Thus the selection of  $a$  and  $b$  may be problem dependent. In some cases, we can select the integration area to be either  $\Omega(0, a)$  or  $\Omega(b, 0)$  in order to get the correct Euler number.

Denote the Euler number as  $E(b, a)$ , corresponding to the integration region  $\Omega(a, b)$ ; in order to see the impact of  $a$  and  $b$ , we employ the following algorithm in our numerical simulations.

ALGORITHM: PARAMETER AUTOSELECTION FOR  $a$ . Given a phase field function  $\phi$  defined on region  $\Omega$ , select  $a$  relatively far away from 0 (for instance,  $a = 1$ ). Select a tolerance number  $\nu$  (for instance,  $\nu = 0.1$ ) and a small step  $h$  (we can use, as an example,  $h = a/50$ ).

- Step 1. If  $|E(0, a) - E(0, a/2)| < \nu$ , exit; else set  $a = a - h$ .
- Step 2. If  $a < h$ , exit with  $a = 0$ ; else loop back to Step 1.

The above algorithm is used to select the best  $a$ . A similar algorithm can be used to select the best  $b$ . A bisection method can be adopted to make the autoselection more efficient. The resulting  $a$  and  $b$  are used to compute the correct Euler numbers. As verified in the earlier theorems, the above algorithm is assured to terminate with suitable  $a$  and  $b$  if the step size  $h$  and the tolerance  $\nu$  are chosen to be reasonably small.

**2.5. Formula simplification.** The formulae given in the above discussion of the Euler number are computable numerically, but for many practical situations they can be further simplified if some appropriate ansatz can be taken. We now discuss some of these simplifications.

First let us take the ansatz

$$(2.10) \quad \phi = \tanh\left(\frac{d}{\sqrt{2}\epsilon}\right) = p\left(\frac{d}{\sqrt{2}\epsilon}\right),$$

which is actually an accurate description of the phase field function in many models such as the basic Allen–Cahn (Ginzburg–Landau) equations, which are popular prototype phase field models for interface and microstructure evolution. Such an ansatz also captures well the phase field function in our energetic phase field model of the vesicle membranes under bending elastic energy.

With such an ansatz, we have the following theorem.

**THEOREM 2.3.** *As in Theorem 2.1, if  $\phi = \tanh(\frac{d}{\sqrt{2}\epsilon}) = p(\frac{d}{\sqrt{2}\epsilon})$ , we have the following:*

*3-d case: Let*

$$(2.11) \quad M_{ij} = \sqrt{\frac{3\epsilon}{8\sqrt{2}\pi}} \left( \nabla_{ij}^2 \phi + \frac{2\phi}{1-\phi^2} \nabla_i \phi \nabla_j \phi \right)$$

*and  $\Lambda(M)$  be defined as before. The Euler number of  $\Gamma$  is given by*

$$(2.12) \quad \frac{\chi}{2} = \lim_{\epsilon \rightarrow 0} \int_{\Omega} \Lambda(M(x)) dx.$$

*2-d case: The Euler number of  $\Gamma$  is given by*

$$(2.13) \quad \chi = \lim_{\epsilon \rightarrow 0} \frac{1}{4\pi} \int_{\Omega} \left( -\Delta \phi + \frac{1}{\epsilon^2} (\phi^2 - 1)\phi \right) dx.$$

**Remark 2.4.** Based on the ansatz (2.10), we have that

$$(2.14) \quad p' = 1 - p, \quad p'' = (p - 1)p.$$

Hence each term in the matrix  $M$  is in fact nonsingular.

*Proof.* A direct calculation shows that

$$\nabla\phi = p' \frac{1}{\sqrt{2\epsilon}} \nabla d, \quad \nabla_{ij}^2 \phi = p'' \frac{1}{2\epsilon^2} \nabla_i d \nabla_j d + p' \frac{1}{\sqrt{2\epsilon}} \nabla^2 d,$$

and

$$\nabla^2 d = \frac{\sqrt{2\epsilon} \nabla^2 \phi}{p'} - \frac{p''}{\sqrt{2\epsilon} p'} \nabla_i d \nabla_j d.$$

Several elementary facts are in order:

$$p'(x) = \tanh'(x) = 1 - \tanh^2(x) = 1 - p^2(x), \quad p'' = -2p(1 - p^2), \quad p''' = -2pp'.$$

Since  $\nabla d = \sqrt{2\epsilon} \nabla \phi / p'$ , we have

$$\begin{aligned} \nabla^2 d &= \frac{\sqrt{2\epsilon} \nabla^2 \phi}{p'} - \frac{p''}{\sqrt{2\epsilon} p'} \nabla_i d \nabla_j d = \sqrt{2\epsilon} \frac{\nabla^2 \phi}{p'} + \sqrt{2\epsilon} \frac{2p}{(1 - p^2)^2} \nabla_i \phi \nabla_j \phi \\ &= \frac{\sqrt{2\epsilon}}{1 - p^2} \left( \nabla^2 \phi + \frac{2p}{1 - p^2} \nabla_i \phi \nabla_j \phi \right) = \frac{\sqrt{2\epsilon}}{1 - \phi^2} \left( \nabla^2 \phi + \frac{2\phi}{1 - \phi^2} \nabla_i \phi \nabla_j \phi \right). \end{aligned}$$

Simple calculation yields that

$$\int_{-\infty}^{+\infty} (1 - \phi^2)^2 dx = \sqrt{2\epsilon} \int_{-\infty}^{+\infty} (1 - \tanh^2(x))^2 dx = \frac{4\sqrt{2\epsilon}}{3}.$$

With sufficiently small  $\epsilon$ , the function  $\phi$  goes to 1 or  $-1$  very quickly (exponentially) away from  $\Gamma$ . Thus, we can just take  $a = -b = 1$  with  $\epsilon \rightarrow 0$ , and the matrix in the formula (2.2) becomes

$$M = \sqrt{\frac{3\epsilon}{8\sqrt{2\pi}}} \left( \nabla^2 \phi + \frac{2\phi}{1 - \phi^2} \nabla_i \phi \nabla_j \phi \right),$$

and (2.12) holds.

For the 2-D cases, by taking a similar ansatz and putting

$$|\nabla \phi|^2 = \frac{1}{2\epsilon^2} (1 - \phi^2)^2$$

into formula (2.7), we finally have (2.13).  $\square$

More simplifications can be made for problems where periodic boundary conditions are used, since  $\int_{\Omega} \Delta \phi = 0$ ; the above formula can be further simplified to

$$(2.15) \quad \chi \approx \frac{1}{4\pi\epsilon^2} \int_{\Omega} (\phi^2 - 1) \phi \, dx.$$

The above formula can be compared with the formula (2.7) (with  $a = -b = 1$ ) applied to the periodic boundary condition case:

$$\begin{aligned} \chi &= \frac{1}{4\pi} \int_{\Omega} \frac{\nabla |\nabla \phi|^2 \cdot \nabla \phi}{2|\nabla \phi|^2} \, dx = \frac{1}{8\pi} \int_{\Omega} \nabla \ln |\nabla \phi|^2 \cdot \nabla \phi \, dx \\ (2.16) \quad &= -\frac{1}{8\pi} \int_{\Omega} \Delta \phi \ln |\nabla \phi|^2 \, dx, \end{aligned}$$

where we need only  $p$  being monotone from  $-1$  to  $1$  in  $\Omega$  instead of being a strictly tanh function.

The previous formula (2.15) has no derivative terms, while the latter one in (2.16) involves no bulk part.

We note that the approximations in (2.12), (2.13), and (2.15) are of spectral accuracy with  $\epsilon \rightarrow 0$ .

*Remark 2.5.* We note that it is possible to get simplified formulae of other types with the ansatz (2.10). For instance, in the 3-D case, let

$$(2.17) \quad \tilde{M}_{ij}(\phi) = \sqrt{\frac{35\epsilon}{64\sqrt{2\pi}}} \left( (1 - \phi^2)\nabla^2\phi + 2\phi\nabla_i\phi\nabla_j\phi \right).$$

Then, the Euler number of the surface  $\Gamma$  in the phase field formulation can also be given by

$$(2.18) \quad \frac{\chi}{2} = \lim_{\epsilon \rightarrow 0} \int_{\Omega} \Lambda(\tilde{M}(\phi)) dx.$$

Note that the change of the constant factors in front of the matrices in (2.11) and (2.17) are due to the use of different weight functions  $(1 - \tanh^2(x))^2$  and  $(1 - \tanh^2(x))^4$  in the derivation.

**2.6. Formulae for cylindrically symmetric membranes.** In [19], we have used the energetic phase field models to compute 3-D vesicle membranes minimizing the bending elastic energy. The numerical examples are for cylindrically symmetric membranes with various different topologies. We now present the Euler number computation in such situations.

In the numerical simulations given in [19], where  $\phi(x) \rightarrow \tanh(\frac{d(x,\Gamma)}{\sqrt{2\epsilon}})$  as  $\epsilon \rightarrow 0$ , the conventional cylindrical coordinates  $(r, \theta, z)$  are used. Suppose that the membrane is rotationally invariant with respect to the  $z$ -axis, i.e.,  $\phi = \phi(z, r, \theta) = \phi(z, r)$ ; then

$$(2.19) \quad \nabla\phi = \begin{pmatrix} \partial_z\phi \\ \partial_r\phi \\ 0 \end{pmatrix}, \quad \nabla_i\phi\nabla_j\phi = \begin{pmatrix} (\partial_z\phi)^2 & \partial_z\phi\partial_r\phi & 0 \\ \partial_z\phi\partial_r\phi & (\partial_r\phi)^2 & 0 \\ 0 & 0 & 0 \end{pmatrix},$$

and

$$(2.20) \quad \nabla^2\phi = \begin{pmatrix} \partial_{zz}^2\phi & \partial_{zr}^2\phi & 0 \\ \partial_{zr}^2\phi & \partial_{rr}^2\phi & 0 \\ 0 & 0 & \frac{1}{r}\partial_r\phi \end{pmatrix}.$$

If we substitute (2.19) and (2.20) into (2.11), we have that

$$M = \sqrt{\frac{3\epsilon}{8\sqrt{2\pi}}} \begin{pmatrix} \partial_{zz}^2\phi + \frac{2\phi}{1-\phi^2}(\partial_z\phi)^2 & \partial_{zr}^2\phi + \frac{2\phi}{1-\phi^2}\partial_z\phi\partial_r\phi & 0 \\ \partial_{zr}^2\phi + \frac{2\phi}{1-\phi^2}\partial_z\phi\partial_r\phi & \partial_{rr}^2\phi + \frac{2\phi}{1-\phi^2}(\partial_r\phi)^2 & 0 \\ 0 & 0 & \frac{1}{r}\partial_r\phi \end{pmatrix}.$$

Hence  $F$ , the sum of the determinants of all principal  $2 \times 2$  minors, is equal to

$$(2.21) \quad F(r, z) = \frac{3\epsilon}{8\sqrt{2\pi}r} \partial_r\phi \left\{ \partial_{zz}^2\phi + \partial_{rr}^2\phi + \frac{2\phi}{1-\phi^2} [(\partial_z\phi)^2 + (\partial_r\phi)^2] \right\},$$

and

$$\begin{aligned}
 \frac{\chi}{2} &\approx \int \int 2\pi r F(r, z) \, dr dz \\
 &\approx \frac{3\epsilon}{4\sqrt{2}} \int \int \partial_r \phi \left\{ \partial_{zz}^2 \phi + \partial_{rr}^2 \phi + \frac{2\phi}{1-\phi^2} [(\partial_z \phi)^2 + (\partial_r \phi)^2] \right\} \, dr dz \\
 (2.22) \quad &\approx \frac{3\epsilon}{4\sqrt{2}} \int \int \partial_r \phi \left\{ \Delta \phi + \frac{2\phi}{1-\phi^2} |\nabla \phi|^2 \right\} \, dr dz,
 \end{aligned}$$

where the operators  $\nabla$  and  $\Delta$  are taken in the  $r$ - $z$  plane.

If we do not take the ansatz  $\phi = \tanh(\frac{d}{\sqrt{2}\epsilon})$ , but simply take (2.19) and (2.20) into the formula (2.2), we get a similar formula in the more general case:

$$\frac{\chi}{2} = \frac{1}{4\pi(a-b)} \int_{\Omega(a,b)} \frac{1}{r} \frac{1}{|\nabla \phi|} \partial_r \phi \left\{ \partial_{zz}^2 \phi + \partial_{rr}^2 \phi - \frac{\nabla |\nabla \phi|^2 \cdot \nabla \phi}{2|\nabla \phi|^4} [(\partial_z \phi)^2 + (\partial_r \phi)^2] \right\} \, dx,$$

or

$$(2.23) \quad \frac{\chi}{2} = \frac{1}{2(a-b)} \int \int_{\Omega(a,b)} \frac{1}{|\nabla \phi|} \partial_r \phi \left\{ \Delta \phi - \frac{\nabla |\nabla \phi|^2 \cdot \nabla \phi}{2|\nabla \phi|^2} \right\} \, dr dz.$$

We remark here that in the 3-D cylindrically symmetric case, the two curvatures can be calculated by

$$(2.24) \quad k_1 = \Delta \phi - \frac{\nabla |\nabla \phi|^2 \cdot \nabla \phi}{2|\nabla \phi|^2},$$

$$(2.25) \quad k_2 = \frac{\partial_r \phi}{r|\nabla \phi|},$$

respectively. One can also use them to derive the formula for the Euler number directly.

Using the partial derivatives, (2.23) can be written as

$$(2.26) \quad \frac{\chi}{2} = \int \int_{\Omega(a,b)} \frac{\partial_r \phi (\partial_{rr}^2 \phi (\partial_z \phi)^2 + \partial_{zz}^2 \phi (\partial_r \phi)^2 - 2\partial_r \phi \partial_z \phi \partial_{rz}^2 \phi)}{2(a-b)((\partial_r \phi)^2 + (\partial_z \phi)^2)^{\frac{3}{2}}} \, dr dz.$$

Using the difference approximation as described in [19], the above integrals can be readily evaluated numerically on a spatial grid.

**3. Numerical realizations.** In section 2, various formulae were presented for calculating the Euler number in two and three dimensions under different kinds of conditions. In general, we can apply finite difference or spectral methods directly to those formulae to calculate the Euler number. However, as discussed in section 2.3, the singular cases often happen in the process with topology changes, such as surface entanglement. When we apply the Euler number formulae to those singular cases, the numerical values at the singular vertices are always very large, which make the final results inaccurate.

Figure 3.1 illustrates a 3-D singular case. The right-most panel shows the function  $F(r, z)$  in formula (2.21) with the  $r$  and  $z$  coordinates. From the right-most graph, we see the numerical value may even go up to 10,000. If the Euler number is calculated directly by formula (2.23), although the theoretical value for this shape is 0.7500, we get 1.0671 which is close to the value 1, the Euler number of a sphere.

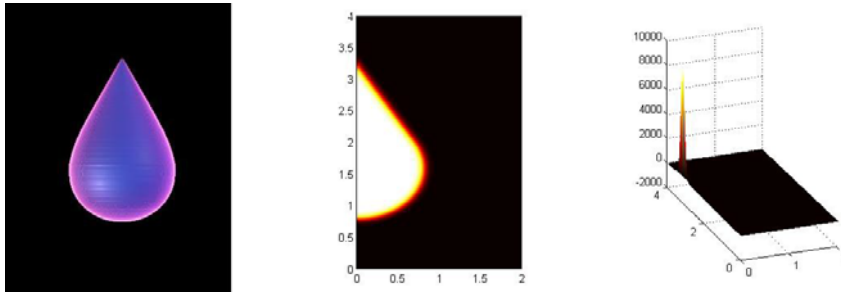


FIG. 3.1. *Singular values at the singular vertex. From left to right: the 3-D picture, the 2-D axis symmetrical r-z planar section, and the singular value around the singular vertex.*

This phenomenon is due to the so-called *singularity compensation* discussed earlier. Because of the finite discrete grid adopted in the numerical scheme, the curvature value at a singular vertex is always regularized from  $\infty$  to a finite number. And in our case, such a change to the finite number provides certain *compensation* to the total Euler number, which can be viewed as putting a small elbow with a large curvature to complement the shape so that the singular shape changes to a regular shape.

A simple but effective way for getting rid of this singularity compensation is to avoid integrating over those singular vertices which are easy to detect, because the numerical values of the integrand at those locations are very big relative to other points. From the formula (2.4), we know that

$$\Lambda(M(x)) = \frac{1}{4\pi(a-b)} p'(d(x, \Gamma)) K(x),$$

where  $K(x)$  is the Gaussian curvature at a point  $x$ . If  $p(x) = \tanh(x/(\sqrt{2}\epsilon))$ ,  $p'(d(x, \Gamma)) = (1 - p^2(d(x, \Gamma)))/(\sqrt{2}\epsilon)$ , then

$$|\Lambda(M(x))| \leq \frac{1}{4\sqrt{2}\pi\epsilon(a-b)} K(x).$$

In most cases, it is easy to estimate the possible largest Gaussian curvature value. In the phase field models, the radius of the smallest ball should be at least larger than the band width  $\epsilon$ . Thus it is natural to choose  $K < 1/\epsilon^2$  for the regular points and regard the singular points as those satisfying the condition  $\Lambda(M(x)) > 1/(4\epsilon^3\sqrt{2}\pi(a-b))$ .

We verify the above argument using the examples shown in Figure 3.2, which represent the same cylindrically symmetric membrane with a singularity at the upper tip whose Euler number can be calculated by formula (2.26). By excluding the singular points with  $\Lambda(M(x)) > 200$ , based on a  $100 \times 200$  grid with  $h = 0.01$ ,  $\epsilon = 2h = 0.02$ , and  $\alpha = \frac{\pi}{6}$ , the computed Euler number we get is 0.7498, which is a very good approximation of the theoretical value 0.7500 obtained from formula (2.9). For  $\alpha = \frac{\pi}{4}$ , the computed Euler number 0.8534 is again an accurate approximation of the theoretical value 0.8536.

In the following section, we apply this technique to all our experiments.

**4. Applications to some phase field models.** In this section, we present two applications of the Euler number developed in the earlier sections for general phase field models. The special examples include the deformation of vesicle membrane configurations minimizing the bending elastic energy and the coarsening of two

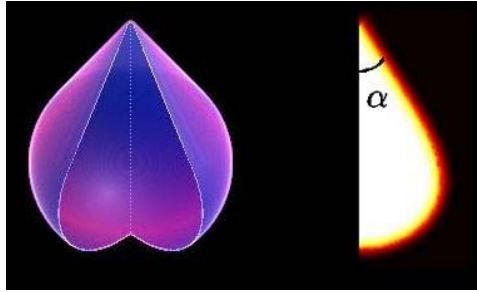


FIG. 3.2. A special cylindrically symmetric membrane with a singular point.

Newtonian bubbles in another Newtonian fluid. We expect that our formula can be equally applied to other more complicated and physical examples involving the phase field models as well.

**4.1. The model for membranes minimizing the bending elastic energy.**

We now consider the problem of minimizing the bending elastic energy:

$$(4.1) \quad E_{\text{elastic}} = \int_{\Gamma} \frac{k}{2} H^2 ds,$$

with area and volume constraints. Here,  $H = (k_1 + k_2)/2$  is the mean curvature of the membrane surface, with  $k_1$  and  $k_2$  as the principal curvatures.  $k$  is the bending rigidity, which can depend on the local heterogeneous concentration of the species (such as protein molecules on the blood cells).

The energetic phase field model studied in [19] is given by the solution of the following modified elastic energy:

$$(4.2) \quad W(\phi) = \int_{\Omega} \frac{k\epsilon}{2} \left| \Delta\phi - \frac{1}{\epsilon^2}(\phi^2 - 1)\phi \right|^2 dx.$$

As  $\epsilon$  is taken asymptotically to zero, the minimum of the energy  $W$  approaches the original energy (4.1). Moreover, at least when the membrane  $\Gamma$ , viewed as a surface in  $\Omega$ , is regular enough, we have

$$(4.3) \quad \phi(x) \simeq \tanh\left(\frac{d(x, \Gamma)}{\sqrt{2}\epsilon}\right) + O(\epsilon^2)$$

approximately satisfied for all  $x \in \Omega$ . Here,  $d = d(x, \Gamma)$  is the distance of the point  $x \in \Omega$  to the surface  $\Gamma$ . Furthermore, the functional

$$(4.4) \quad A = \int_{\Omega} \phi(x) dx$$

goes to the difference of interior volume and exterior volume, and the function

$$(4.5) \quad B = \int_{\Omega} \left[ \frac{\epsilon}{2} |\nabla\phi|^2 + \frac{1}{4\epsilon} (\phi^2 - 1)^2 \right] dx$$

approaches  $2\sqrt{2} \text{area}(\Gamma)/3$ , or about 0.94 times the area of  $\Gamma$ . We note that for energy minimizing functions,

$$\int_{\Omega} \frac{\epsilon}{2} |\nabla\phi|^2 dx \approx \int_{\Omega} \frac{1}{4\epsilon} (\phi^2 - 1)^2 dx.$$

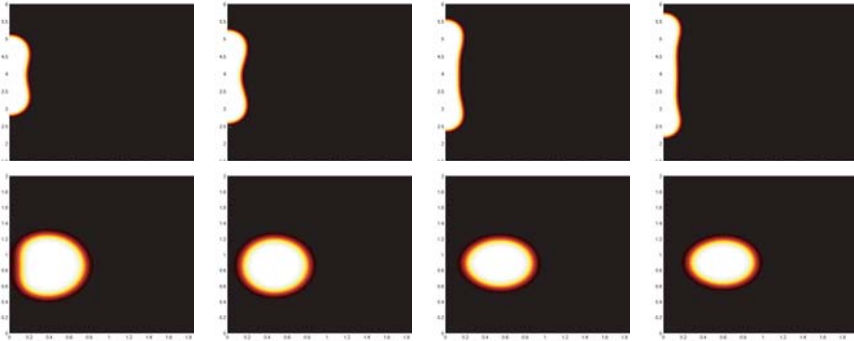


FIG. 4.1. Deformation of a gourd (top) and a torus (bottom) with areas at 5.834, 6.258, 6.682, and 7.000. Pictures are displayed in different scales for best view.

Thus, it is also convenient to take

$$B = \int_{\Omega} \epsilon |\nabla \phi|^2 dx$$

as the constraint for numerical purposes. For a more detailed asymptotic analysis and a more rigorous convergence analysis, including the convergence of the Euler Lagrange equation, we refer to our subsequent work [17].

It has come to our attention recently that the unconstrained variational approach of using (4.2) to approximate the 2-D Willmore functional (4.1) was also previously used, by the name of a relaxed formulation, in the application of image inpainting (see [23, 10, 32] and the references cited therein). This relaxed formulation was motivated by the  $\Gamma$ -convergence framework of De Giorgi [14] (see also [32]) for general variational problems, although the convergence of such a formulation remains to be rigorously justified.

The numerical simulations in [19] were aimed at the study of the minimizers of the elastic energy  $W(\phi)$  under given surface area and volume. By scaling invariance, the volume can be fixed to be a constant, while the area is changed continuously to probe the energy landscape. A set of bubble shapes was discovered, and topological changes were observed along the way only when the configurations were visualized. Our objective here is to show that the Euler number formula (2.26) can be used as an effective tool to automatically detect the topological changes.

The detailed numerical algorithms and numerical simulations of the branches of membrane shape deformations have been presented in [19].

Figure 4.1 shows the deformation of a gourd (the first row, computed with a  $40 \times 375$  grid and  $\epsilon = 1.5h = 0.03$ ) and a torus (the second row,  $100 \times 100$  grid,  $\epsilon = 1.5h = 0.03$ ) with increasing surface areas, with volumes fixed at 1.1000. The gourd becomes thinner, and the torus moves further away from its axis. It is obvious that there is no topological change for both the gourd and the torus. This can be seen from the graph of the Euler numbers (Figure 4.2) with the value being kept at 1 for the gourd and 0 for the torus. On the other hand, in the same figure, the graphs of their energy are two intersecting curves, which illustrates the existence of two shapes with totally different topologies but the same energy.

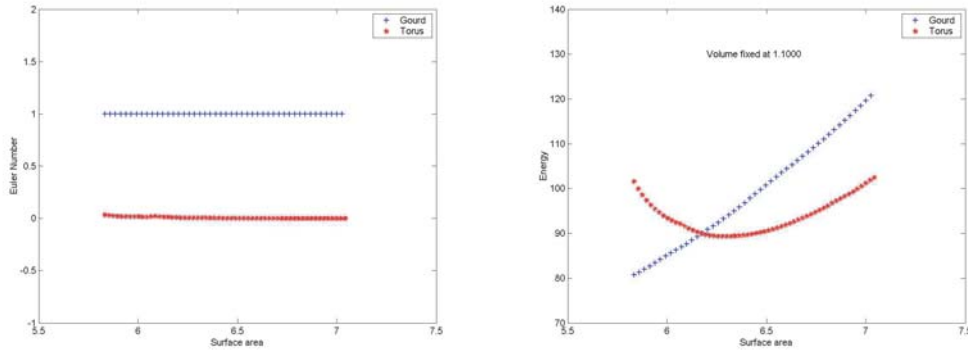


FIG. 4.2. The energy (left) and the computed Euler number (right) of gourd and torus shapes.

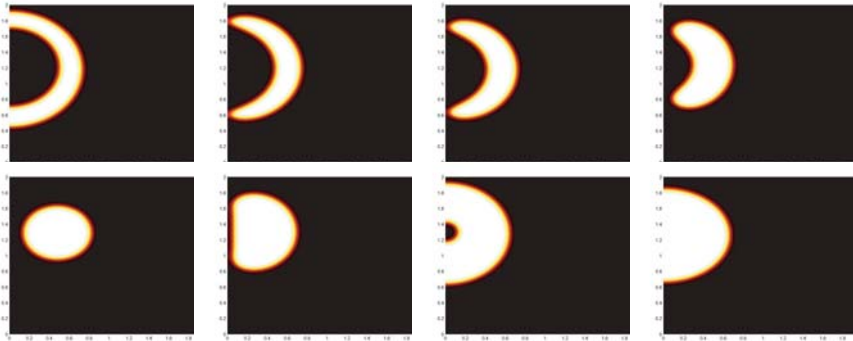


FIG. 4.3. Deformation of a shell to a pitomba, a bangle, a torus, a longan and finally a ball (cross section view) with areas valued at 9.811, 9.546, 8.485, 6.894, 6.364, 5.515, 5.303, and 5.091.

In the next set of numerical simulations, a rectangular domain with a  $100 \times 200$  Cartesian grid, with  $h = 0.01$ , is used and  $\epsilon = 2h = 0.02$ . Figure 4.3 shows the shape deformations with a decreasing area from 11.2960 to 5.0912 while fixing the volume at 1.1000. The left picture in Figure 4.4 shows the corresponding change of the bending energy with different surface areas. Good resolutions of the interfaces based on the above choices of the computational grid and the parameter values have been demonstrated in [19] for such a solution branch.

In the whole energy minimizing process, the shape always jumps from one branch to another, which results in a discontinuous energy curve. Here the shape of the vesicle changes from a shell to a bangle (with no obvious energy jump), then to a torus (with a noticeable energy jump at the surface area  $\beta = 6.6822$ ), then a longan (with an energy jump at around  $\beta = 5.3563$ ), and finally to a spherical ball (an energy jump at around  $\beta = 5.1442$ ). There are three topological changes during the shape deformation: (1) from shell to a bangle, (2) from torus to a longan, and (3) from longan to a spherical ball. The energy can hardly detect the change from shell to bangle, despite the occurrence of the topology change.

The right picture in Figure 4.4 shows the change of the computed Euler numbers. The graph has exactly three jumps corresponding to the three topological changes. We can see the corresponding Euler numbers 2, 0, 2, and 1 for shell, torus, longan,

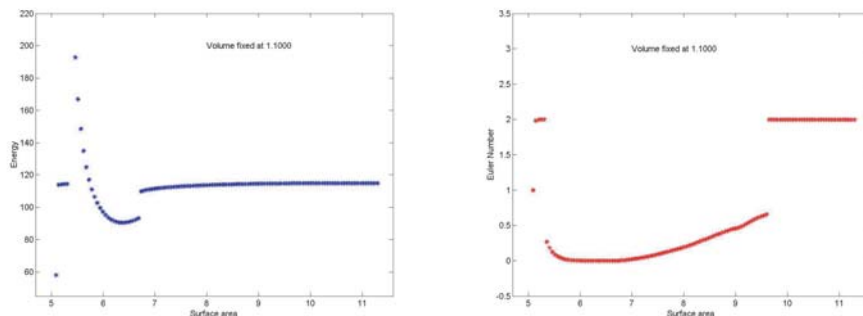


FIG. 4.4. The energy (left) and the computed Euler number (right) for the deformation of a shell shape with decreasing area.

and ball shapes, respectively.

The calculation of the Euler numbers used the autoselection algorithm for the best parameters  $a$  and  $b$ . Observing the second, third, and sixth graphs of Figure 4.3 carefully, it is not hard to understand why we need such an algorithm here, based on the theory stated in section 2.4. As different shapes have different best values of  $a$  and  $b$ , we thus have different integration areas for the Euler numbers. It may be noticeable that some values are not exactly 0 when the vesicle surface area belongs to the interval  $[5.3, 9.8]$ . Such small errors are mainly due to the approximation errors of the finite difference scheme and the integration scheme. Fortunately, those errors are always sufficiently small (less than 0.1 in this case) to be distinguishable from the Euler number jumps, which are at least 1. This makes our method very stable and sensitive in detecting the topology changes.

In summary, the above experiments demonstrate that our formula for the Euler number can be successfully used to retrieve topological information and to capture topological events. Of course, the Euler number alone does not completely determine the topology of the interface.

**4.2. The phase field model of fluid bubble motion.** In the study of the coarsening of the Newtonian bubbles in another Newtonian fluid, the following 2-D simple problem has been considered:

$$(4.6) \quad \begin{cases} \frac{\partial u}{\partial t} + (u \cdot \nabla)u - \nu \nabla \cdot D(u) + \nabla p + \lambda \nabla \cdot (\nabla \phi \odot \nabla \phi) = 0, & (x, t) \in Q_T, \\ \nabla \cdot u = 0, & (x, t) \in Q_T, \\ \frac{\partial \phi}{\partial t} + (u \cdot \nabla)\phi - \gamma \Delta(\Delta \phi + f(\phi)) = 0, & (x, t) \in Q_T, \end{cases}$$

with the initial values  $u(x, 0) = u_0(x)$ ,  $d(x, 0) = d_0(x)$  and periodic boundary conditions. Here  $f(\phi) = (1 - \phi^2)\phi/\epsilon^2$ ,  $D(u) = (\nabla u + (\nabla u)^T)/2$ ,  $\nabla \phi \odot \nabla \phi$  is the induced elastic tensor, with the  $(j, k)$ th entry being  $\partial_{x_j} \phi \partial_{x_k} \phi$ . The above equations have been used in [28] to analyze the motion of bubbles in a Newtonian fluid. These phase field models are also very similar to the liquid crystal model studied in [20, 27, 29].

The above simple system was used to study the free interface motion under the surface tension in the mixture of two Newtonian fluids with the same density and viscosity constants [1, 2, 3, 4, 5, 15, 21, 25, 26, 28, 30, 31, 33, 36, 40]. The system

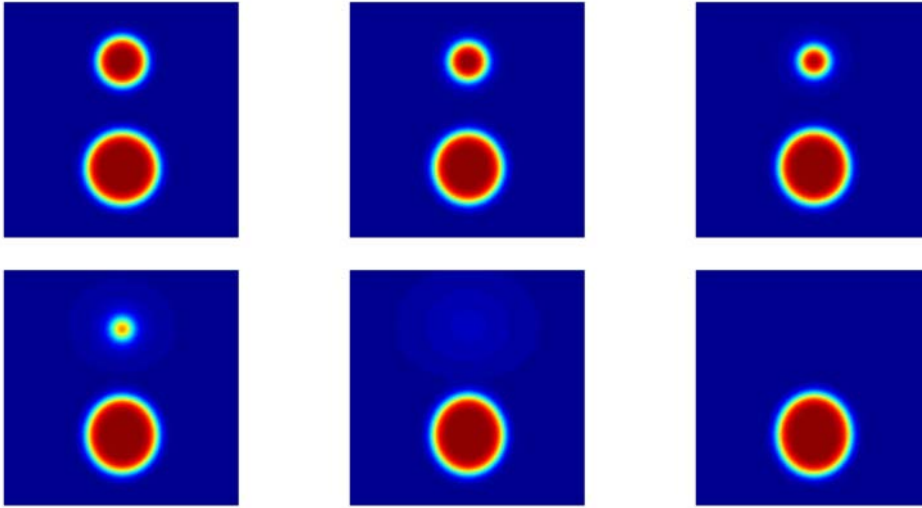


FIG. 4.5. Deformation of two bubbles in a Newtonian fluid with the time valued at 0.00, 0.10, 0.18, 0.22, 0.24, 0.28.

satisfies the following energy law:

$$(4.7) \quad \frac{d}{dt} \int_{\Omega} \left\{ \frac{1}{2} |u|^2 + \frac{\lambda}{2} |\nabla \phi|^2 + \lambda F(\phi) \right\} dx = - \int_{\Omega} \{ \nu |\nabla u|^2 + \gamma \lambda |\nabla (\Delta \phi - f(\phi))|^2 \} dx.$$

Moreover, the whole system can be viewed as the approximation of the classical sharp interface model with the kinematic and traction-free boundary condition on the free interface [28]. As the transition width  $\epsilon$  approaches zero, the induced bulk elastic stress term converges to the corresponding surface tension.

To test our formula for computing the Euler number, we solve the above system in two space dimensions via a spectral spatial discretization coupled with a second order semi-implicit-in-time scheme for  $\phi$  and a semi-implicit projection scheme for the Navier–Stokes equations, such as those in [20, 28].

Figure 4.5 shows a special example of the deformation of two Newtonian bubbles in another Newtonian fluid. In this experiment, we take the  $128 \times 128$  grid, period boundary condition on area  $[0, 2\pi] \times [0, 2\pi]$ , and  $\epsilon = 2.5h = 0.1227$ ,  $\lambda = 10.0$ ,  $\gamma = 3.0$ ,  $\nu = 1.0$ . In the simulation, the larger bubble grows at the expense of the shrinkage of the smaller one. In fact, the smaller bubble dissolves into the fluid, while the bigger bubble absorbs from the fluid, similar to the well-known Oswald ripening effects (due to the Cahn–Hilliard effect of the phase equation in (4.6)). The total volume of these two bubbles remains constant in time.

The topology change in this simulation can be characterized by the Euler number of the whole configuration. At the beginning, the Euler number of the configuration with the two bubbles is 2. And finally, after the smaller bubble is totally absorbed by the larger bubble, the Euler number of the bubble configuration becomes 1. Figure 4.6 shows the sharp change in the Euler number in this procedure using the formula (2.16).

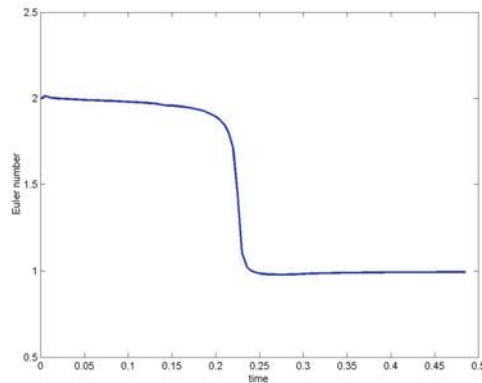


FIG. 4.6. A plot of the Euler number in time with the annihilation of the small bubble.

**5. Conclusion.** While an important advantage of phase field modeling of the interface variation and the interfacial motion is its ability to handle the change of interface topologies in natural and physically meaningful ways, it has also come to our attention that in many practical problems, useful topological information may be needed, and the effective control of the topological transformations may be important. In this paper, mechanisms to retrieve relevant topological information based on the phase field formulations are discussed. In particular, some robust formulae for computing a generalized Euler number of the interface are proposed based on the phase field order parameter  $\phi$ . Using a special ansatz, we also get further simplified formulae. For smooth interfaces, our formulae give desired quantized characterization of the interface genus. When passing through singularities, they give fractional values that generalize the notion of the genus.

As a demonstration, numerical experiments are performed for the cases of a static deformation of a 3-D axial symmetric membrane as well as a time dependent annihilation of fluid bubbles in 2-D space. The experimental results show that the proposed methods for computing the Euler number are very effective and robust in detecting the topological changes. The ideas presented in this paper are very natural and easy to implement for other phase field models and may also be equally applicable to other simulation methods for free boundary and interface problems including the standard level set methods. Rigorous analysis of the formulae derived here based on formal asymptotic analysis are currently underway [17]. We are also working on the problem of taking the Euler number as a constraint within the phase field framework to study and analyze mechanisms in a physical system for controlling and preventing topological changes, should they become desirable.

#### REFERENCES

- [1] D. M. ANDERSON AND G. B. MCFADDEN, *A diffuse-interface description of internal waves in a near-critical fluid*, Phys. Fluids, 9 (1997), pp. 1870–1879.
- [2] D. M. ANDERSON, G. B. MCFADDEN, AND A. A. WHEELER, *Diffuse-interface methods in fluid mechanics*, Ann. Rev. Fluid Mech., 30 (1998), pp. 139–165.
- [3] T. BLESGEN, *A generalization of the Navier–Stokes equations to two phase flow*, J. Phys. D Appl. Phys., 32 (1999), pp. 1119–1123.

- [4] F. BOYER, *Mathematical study of multi-phase flow under shear through order parameter formulation*, *Asymptot. Anal.*, 20 (1999), pp. 175–212.
- [5] F. BOYER, *A theoretical and numerical model for the study of incompressible mixture flows*, *Comput. & Fluids*, 31 (2002), pp. 41–68.
- [6] G. CAGINALP, *An analysis of a phase field model of a free boundary*, *Arch. Ration. Mech. Anal.*, 92 (1986), pp. 205–245.
- [7] J. W. CAHN AND S. M. ALLEN, *A microscopic theory for domain wall motion and its experimental verification in Fe-Al alloy domain growth kinetics*, *J. Phys. Colloque*, C7 (1977), pp. 51–54.
- [8] J. W. CAHN, C. M. ELLIOTT, AND A. NOVICK-COHEN, *The Cahn–Hilliard equation with a concentration dependent mobility: Motion by minus the Laplacian of the mean curvature*, *European J. Appl. Math.* 7 (1996), pp. 287–301.
- [9] J. W. CAHN AND J. E. HILLARD, *Free energy of a nonuniform system. I. Interfacial free energy*, *J. Chem. Phys.*, 28 (1958), pp. 258–267.
- [10] T. F. CHAN, S. H. KANG, AND J. SHEN, *Euler’s elastica and curvature-based inpainting*, *SIAM J. Appl. Math.*, 63 (2002), pp. 564–592.
- [11] Y. C. CHANG, T. Y. HOU, B. MERRIMAN, AND S. OSHER, *A level set formulation of Eulerian interface capturing methods for incompressible fluid flows.*, *J. Comput. Phys.*, 124 (1996), pp. 449–464.
- [12] L.-Q. CHEN AND Y.-Z. WANG, *The continuum field approach to modeling microstructural evolution*, *J. Minerals Metals Materials Soc.*, 48 (1996), pp. 13–18.
- [13] L.-Q. CHEN, C. WOLVERTON, V. VAITHYANATHAN AND Z.-K. LIU, *Modeling solid-state phase transformations and microstructure evolution*, *MRS Bulletin*, 26 (2001), pp. 197–202.
- [14] E. DE GIORGI, *Some remarks on Gamma-convergence and least squares method*, in *Composite Media and Homogenization Theory (ICTP, Trieste, 1990)*, G. Dal Maso and G. F. Dell Antonio, eds., Birkhäuser Boston, Cambridge, MA, 1990, pp. 135–142.
- [15] D. L. DENNY AND R. L. PEGO, *Models of low-speed flow for near-critical fluids with gravitational and capillary effects*, *Quart. Appl. Math.*, 58 (2000), pp. 103–125.
- [16] M. P. DO CARMO, *Differential Geometry of Curves and Surfaces*, Prentice–Hall, Englewood Cliffs, NJ, 1976.
- [17] Q. DU, C. LIU, R. RYHAM, AND X. WANG, *A phase field formulation of the Willmore problem*, *Nonlinearity*, 18 (2005), pp. 1249–1267.
- [18] Q. DU, C. LIU, R. RYHAM, AND X. WANG, *Phase field modeling of the spontaneous curvature effect in cell membranes*, *Comm. Pure Appl. Anal.*, 4 (2005), pp. 537–548.
- [19] Q. DU, C. LIU, AND X. WANG, *A phase field approach in the numerical study of the elastic bending energy for vesicle membranes*, *J. Comput. Phys.*, 198 (2004), pp. 450–468.
- [20] Q. DU, B. GUO, AND J. SHEN, *Fourier spectral approximation to a dissipative system modeling the flow of liquid crystals*, *SIAM J. Numer. Anal.*, 39 (2001), pp. 735–762.
- [21] J. E. DUNN AND J. SERRIN, *On the thermomechanics of interstitial working*, *Arch. Ration. Mech. Anal.*, 88 (1985), pp. 95–133.
- [22] C. M. ELLIOTT, *Approximation of curvature dependent interface motion*, in *State of the Art in Numerical Analysis*, I. Duff and G. A. Watson, eds., Clarendon Press, Oxford, UK, 1997, pp. 407–440.
- [23] S. ESEDOGLU AND J. H. SHEN, *Digital inpainting based on the Mumford–Shah–Euler image model*, *European J. Appl. Math.*, 13 (2002), pp. 353–370.
- [24] W. GEORGE AND J. WARREN, *A Parallel 3D dendritic growth simulator using the phase-field method*, *J. Comput. Phys.*, 177 (2002), pp. 264–283.
- [25] M. E. GURTIN, D. POLIGNONE, AND J. VIÑALS, *Two-phase binary fluids and immiscible fluids described by an order parameter*, *Math. Models Methods Appl. Sci.*, 6 (1996), pp. 815–831.
- [26] D. JACQMIN, *Calculation of two-phase Navier–Stokes flows using phase-field modeling*, *J. Comput. Phys.*, 155 (1999), pp. 96–127.
- [27] F. H. LIN AND C. LIU, *Nonparabolic dissipative systems, modeling the flow of liquid crystals*, *Comm. Pure Appl. Math.*, 48 (1995), pp. 501–537.
- [28] C. LIU AND J. SHEN, *A phase field model for the mixture of two incompressible fluids and its approximation by a Fourier-spectral method*, *Phys. D*, 179 (2003), pp. 211–228.
- [29] C. LIU AND N. J. WALKINGTON, *Approximation of liquid crystal flows*, *SIAM J. Numer. Anal.*, 37 (2000), pp. 725–741.
- [30] C. LIU AND N. J. WALKINGTON, *An Eulerian description of fluids containing visco-hyperelastic particles*, *Arch. Ration. Mech. Anal.*, 159 (2001), pp. 229–252.
- [31] J. LOWENGRUB AND L. TRUSKINOVSKY, *Quasi-incompressible Cahn–Hilliard fluids and topological transitions*, *Roy. Soc. London Proc. Ser. A Math. Phys. Eng. Sci.*, 454 (1998), pp. 2617–2654.

- [32] R. MARCH AND M. DOZIO, *A variational method for the recovery of smooth boundaries*, Image & Vision Comput., 15 (1997), pp. 705–712.
- [33] G. B. MCFADDEN, A. A. WHEELER, AND D. M. ANDERSON, *Thin interface asymptotics for an energy/entropy approach to phase-field models with unequal conductivities*, Phys. D, 144 (2000), pp. 154–168.
- [34] G. B. MCFADDEN, A. A. WHEELER, R. J. BRAUN, S. R. CORIELL, AND R. F. SEKERKA, *Phase-field models for anisotropic interfaces*, Phys. Rev. E (3), 48 (1993), pp. 2016–2024.
- [35] W. W. MULLINS AND R. F. SEKERKA, *On the thermodynamics of crystalline solids*, J. Chem. Phys., 82 (1985), pp. 5192–5202.
- [36] T. QIAN, X. P. WANG, AND P. SHENG, *Generalized Navier boundary condition for the moving contact line*, Comm. Math. Sci., 1 (2003), pp. 333–341.
- [37] J. RUBINSTEIN, P. STERNBERG, AND J. B. KELLER, *Reaction-diffusion processes and evolution to harmonic maps*, SIAM J. Appl. Math., 49 (1989), pp. 1722–1733.
- [38] J. E. TAYLOR AND J. W. CAHN, *Linking anisotropic sharp and diffuse surface motion laws via gradient flows*, J. Statist. Phys., 77 (1994), pp. 183–197.
- [39] P. YU, S.-Y. HU, L.-Q. CHEN, AND Q. DU, *An iterative-perturbation scheme for treating inhomogeneous elasticity in phase field models*, J. Comput. Phys., 208 (2005), pp. 34–50.
- [40] P. YUE, J. FENG, C. LIU, AND J. SHEN, *A diffuse-interface method for simulating two-phase flows of complex fluids*, J. Fluid Mech., 515 (2005), pp. 293–317.